Detailed analysis of the tetraquark potential and flip-flop in SU(3) lattice QCD

Fumiko Okiharu

Department of Physics, Nihon University, Kanda-Surugadai 1-8-14, Chiyoda, Tokyo 101-8308, Japan

Hideo Suganuma

Faculty of Science, Tokyo Institute of Technology, Ohokayama 2-12-1, Meguro, Tokyo 152-8551, Japan

Toru T. Takahashi

Yukawa Institute for Theoretical Physics, Kyoto University, Kitashirakawa-Oiwake, Sakyo, Kyoto 606-8502, Japan

We perform the detailed study of the tetraquark (4Q) potential V_{4Q} for various QQ-$\bar{Q}\bar{Q}$ systems in SU(3) lattice QCD with $\beta = 6.0$ and $16^3 \times 32$ at the quenched level. For about 200 different patterns of 4Q systems, V_{4Q} is extracted from the 4Q Wilson loop in 300 gauge configurations, with the smearing method to enhance the ground-state component. We calculate V_{4Q} for planar, twisted, asymmetric, and large-size 4Q configurations, respectively. Here, the calculation for large-size 4Q configurations is done by identifying $16^2 \times 32$ as the spatial size and 16 as the temporal one, and the long-distance confinement force is particularly analyzed in terms of the flux-tube picture. When QQ and $\bar{Q}\bar{Q}$ are well separated, V_{4Q} is found to be expressed as the sum of the one-gluon-exchange Coulomb term and multi-Y-type linear term based on the flux-tube picture. When the nearest quark and antiquark pair is spatially close, the system is described as a "two-meson" state. We observe a flux-tube recombination called a "flip-flop" between the connected 4Q state and the two-meson state around the level-crossing point. This leads to infrared screening of the long-range color forces between (anti)quarks belonging to different mesons, and results in the absence of the color van der Waals force between two mesons.

I. INTRODUCTION

The interquark force is one of the elementary quantities for the study of the multiquark system in the quark model. Since the first application of lattice QCD simulations was done for the interquark potential between a quark and an antiquark using the Wilson loop in 1979 [1], the study of the interquark force has been one of the important issues in lattice QCD [2]. Actually, in hadron physics, the interquark force can be regarded as an elementary quantity to connect "the quark world" to "the hadron world," and plays an important role to hadron properties.

In addition to the $Q\bar{Q}$ potential [1–4], recent lattice QCD studies clarify the three-quark (3Q) potential [5–8], which is responsible to the baryon structure. In fact, our group recently studied the 3Q potential V_{3Q} in detail with lattice QCD, and clarified that it obeys the Coulomb plus Y-type linear potential [5–8]. However, no one knows the interquark force from QCD in the exotic multiquark system such as tetraquark mesons (QQ-$\bar{Q}\bar{Q}$), pentaquark baryons (4Q-$\bar{Q}$), dibaryons (6Q), and so on.

In these years, various candidates of multiquark hadrons have been experimentally observed. $\Theta^+(1540)$ [9–12], $\Xi^{--}(1862)$ [13], and $\Theta_c(3099)$ [14] are considered to be pentaquark (5Q) states [15,16] because of their exotic quantum numbers, although some high-energy experiments report null results [17]. $X(3872)$ [18–21] and $D_s(2317)$ [22,23] are expected to be tetraquark (4Q) states [24–32] from the consideration of their mass, narrow decay width and decay mode.

These discoveries of multiquark hadrons are expected to reveal new aspects of hadron physics, especially for the interquark force such as the quark confinement force, the color-magnetic interaction, and the diquark correlation [33]. According to these experimental results, it is desired to investigate the interquark force in the multiquark system directly based on QCD [34–42], which would present the proper Hamiltonian for the quark-model calculation of multiquarks [43–45].

As for the 4Q candidates, $X(3872)$ was discovered in the process $B^+ \to K^+ + X(3872) \to K^+ + \pi^- \pi^+ J/\psi$ at KEK (Belle) in 2003 [18], and its existence was confirmed by Fermilab (CDF [19], D0 [20]) and SLAC (*BABAR*) [21]. $D_s(2317)$ was also found in the B-$\bar{B}$ reaction at $\Upsilon(4S)$ resonance at SLAC (*BABAR*) [22] and consecutively at KEK (Belle) [23] in 2003. As the unusual features of $X(3872)$, its mass is rather close to the threshold of $D^0(c\bar{u})$ and $\bar{D}^{0*}(u\bar{c})$, and its decay width is very narrow as $\Gamma < 2.3$ MeV (90% C.L.). These facts seem to indicate that $X(3872)$ is a 4Q state [24,25] or a molecular state of $D^0(c\bar{u})$ and $\bar{D}^{0*}(u\bar{c})$ [26–29] rather than an excited state of a $c\bar{c}$ system [30–32]. Also, $D_s(2317)$ cannot be regarded as the simple meson of $c\bar{s}$, but is conjectured to be a 4Q state from the similar reasons on the mass and the narrow decay width.

Also in the light quark sector, the possibility of 4Q hadrons has been pointed out. For instance, Jaffe proposed in 1977 that the light scalar nonet including $f_0(980)$ and $a_0(980)$ can be interpreted as $QQ\bar{Q}\bar{Q}$ rather than $Q\bar{Q}$ [46].

Since then, many studies of the scalar nonet have been done in terms of the 4Q state [47,48].

As an analytical guiding model for the multiquark system, the flux-tube picture [49–56] has been investigated for the structure and the reaction of hadrons and is supported by recent lattice QCD studies [5,6,35–41,57]. In this picture, valence quarks are linked by the color flux tube as a quasi-one-dimensional object. The flux tube has a large string tension of about $\sigma \simeq 0.89$ GeV/fm, and therefore its length is to be minimized. For the multiquark system, this picture predicts an interesting phenomenon of the "flip-flop," i.e., a recombination of the flux-tube configuration so as to minimize the total length of the flux tube in accordance with the change of the quark location [55,56]. This process is important not only for the structure of multiquark systems but also for the reaction process of hadrons.

In this paper, we study the 4Q potential, i.e., the interaction between quarks in the 4Q system directly from QCD by using SU(3) lattice QCD at the quenched level, and investigate the hypothetical flux-tube picture for the multiquark system and the flip-flop in terms of QCD. Here, the lattice QCD Monte Carlo simulation is the first-principle calculation of QCD and is considered as the only reliable method for nonperturbative QCD at present. We note that lattice QCD is also a useful method to select out the correct picture for nonperturbative QCD in the low-energy region through the comparison with the lattice results.

The organization of this paper is as follows. In Sec. II, after a brief review on the lattice studies of static quark potentials, we present a theoretical form for the 4Q potential based on the flux-tube picture. In Sec. III, we present the formalism for the 4Q Wilson loop and the 4Q potential. The lattice QCD results are shown in Sec. IV. In Sec. V, we compare the lattice QCD results with the theoretical form, and discuss the flux-tube picture and the flip-flop. Section VI is devoted to the summary and concluding remarks.

II. THEORETICAL CONSIDERATION FOR THE 4Q POTENTIAL

A. $Q\bar{Q}$, 3Q, and 5Q potentials

To begin with, we give a theoretical consideration for the multiquark potential. From a lot of lattice QCD studies [1–6], the static $Q\bar{Q}$ potential is known to be well described by

$$V_{Q\bar{Q}} = -\frac{A_{Q\bar{Q}}}{r} + \sigma_{Q\bar{Q}}r + C_{Q\bar{Q}}, \qquad (1)$$

where r denotes the distance between the quark and the antiquark. The first term is considered to be the Coulomb term due to the one-gluon exchange (OGE) and $A_{Q\bar{Q}}$ denotes the Coulomb coefficient. The second term is the linear confinement term with the string tension, $\sigma_{Q\bar{Q}} \simeq 0.89$ GeV/fm.

From the recent detailed studies in lattice QCD with ($\beta = 5.7$, $12^3 \times 24$), ($\beta = 5.8$, $16^3 \times 32$), ($\beta = 6.0$, $16^3 \times 32$), and ($\beta = 6.2$, 24^4) [5–8,37–40], the 3Q potential is clarified to be the sum of the OGE Coulomb term and the Y-type linear confinement term as

$$V_{3Q} = -A_{3Q}\sum_{i<j}\frac{1}{|\mathbf{r}_i - \mathbf{r}_j|} + \sigma_{3Q}L_{\min} + C_{3Q}. \qquad (2)$$

Here, $L_{\min}$ denotes the minimal value of the total flux-tube length, which corresponds to the Y-shaped flux tube linking the three quarks. In fact, the lattice data of the 3Q potential, $V_{3Q}^{\rm latt}$, can be well reproduced with only three parameters, A_{3Q}, σ_{3Q}, and C_{3Q}.

To demonstrate the validity of the Y Ansatz, we show in Fig. 1 the lattice QCD data of the 3Q confinement potential $V_{3Q}^{\rm conf}$, i.e., the 3Q potential subtracted by its Coulomb and constant parts,

$$V_{3Q}^{\rm conf} \equiv V_{3Q}^{\rm latt} - \left\{-A_{3Q}\sum_{i<j}\frac{1}{|\mathbf{r}_i - \mathbf{r}_j|} + C_{3Q}\right\}, \qquad (3)$$

plotted against Y-shaped flux-tube length $L_{\min}$, at $\beta = 5.8$, 6.0, and 6.2 in the lattice unit. For each β, clear linear correspondence is found between 3Q confinement potential $V_{3Q}^{\rm conf}$ and $L_{\min}$ as $V_{3Q}^{\rm conf} \simeq \sigma_{3Q}L_{\min}$, which indicates the Y Ansatz for the 3Q potential [38–40].

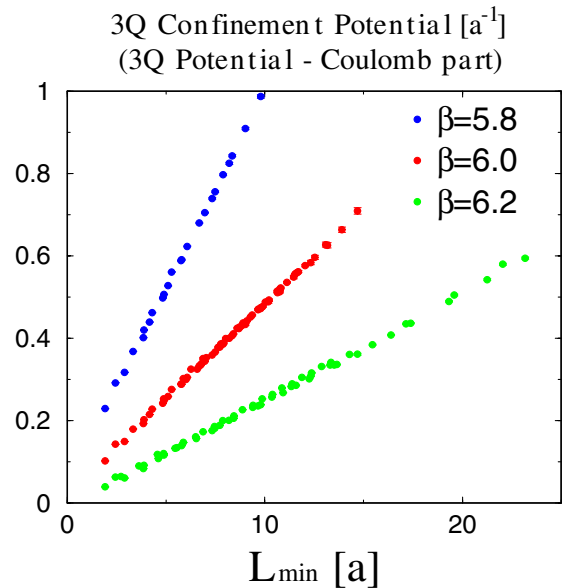This lattice QCD result strongly supports the flux-tube picture for baryons, and the Y-type flux-tube formation is

3Q Confinement Potential [a^{-1}]
(3Q Potential - Coulomb part)

FIG. 1 (color online). The lattice QCD result for the 3Q confinement potential $V_{3Q}^{\rm conf}$, i.e., the 3Q potential subtracted by its Coulomb and constant parts, plotted against Y-shaped flux-tube length $L_{\min}$ at $\beta = 5.8$, 6.0, and 6.2 in the lattice unit. The clear linear correspondence between 3Q confinement potential $V_{3Q}^{\rm conf}$ and $L_{\min}$ indicates the Y Ansatz for the 3Q potential.

actually observed in lattice QCD through the direct measurement of the action density in the presence of spatially fixed three quarks [37–40,57]. The Y Ansatz for the 3Q system is also supported by recent further lattice QCD studies [58,59] and analytical studies [60,61].

As for the relation between $V_{Q\bar{Q}}$ and V_{3Q}, we have found the OGE result $A_{3Q} \simeq \frac{1}{2} A_{Q\bar{Q}}$ and the universality of the string tension $\sigma_{3Q} \simeq \sigma_{Q\bar{Q}}$, which also supports the flux-tube picture [49–56] and the strong-coupling expansion scheme [50,51].

Very recently, the 5Q potential is also studied in lattice QCD [36–42]. It is well described by the OGE Coulomb plus the multi-Y-type linear potential [36–41]. With the minimal length $L_{\min}$ of the flux tube, the 5Q potential can be well described as

$$V_{5Q} = \frac{g^2}{4\pi}\sum_{i<j}\frac{T_i^a T_j^a}{|\mathbf{r}_i - \mathbf{r}_j|} + \sigma_{5Q}L_{\min} + C_{5Q}$$

$$= -A_{5Q}\left\{\left(\frac{1}{r_{12}} + \frac{1}{r_{34}}\right) + \frac{1}{2}\left(\frac{1}{r_{15}} + \frac{1}{r_{25}} + \frac{1}{r_{35}} + \frac{1}{r_{45}}\right)\right.$$

$$\left. + \frac{1}{4}\left(\frac{1}{r_{13}} + \frac{1}{r_{14}} + \frac{1}{r_{23}} + \frac{1}{r_{24}}\right)\right\} + \sigma_{5Q}L_{\min} + C_{5Q},$$

$$(4)$$

with (A_{5Q}, σ_{5Q}) fixed to be (A_{3Q}, σ_{3Q}) following the OGE result and the universality of the string tension. This lattice result also supports the flux-tube picture.

B. Theoretical Ansätze for the 4Q potential

Now, we investigate the theoretical form of the 4Q potential V_{4Q} with respect to the flux-tube picture, which seems workable for $Q\bar{Q}$ mesons and baryons. For the argument of the low-lying 4Q states, we consider the 4Q state of $((QQ)_{\bar{3}}\text{-}(\bar{Q}\bar{Q})_3)_1$ as shown in Fig. 2. Here, $(QQ)_{\bar{3}}$ denotes that two quarks form the $\bar{3}$ representation of the color SU(3). The meaning of $(\bar{Q}\bar{Q})_3$ is similar. By combining $(QQ)_{\bar{3}}$ with $(\bar{Q}\bar{Q})_3$, the 4Q system can be constructed as a color-singlet state. We note that another possible 4Q system of $((QQ)_6 - (\bar{Q}\bar{Q})_{\bar{6}})_1$ is expected to be a highly excited state, since the attractive (repulsive) force acts between quarks, when the QQ cluster belongs to $\bar{3}$ (**6**)
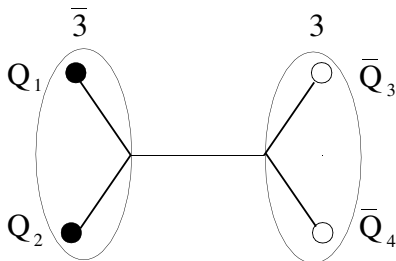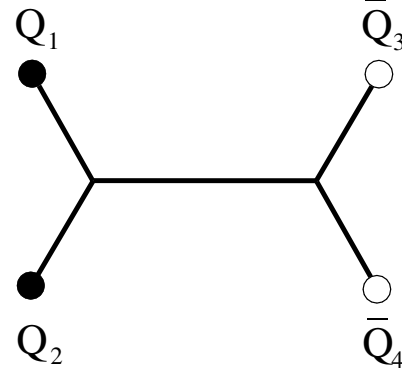
FIG. 3. The connected tetraquark system. All quarks and antiquarks are connected with the single flux tube, which is double-Y-shaped.

representation in a perturbative sense, which leads to the $\bar{3}$ diquark picture [33].

In the flux-tube picture, the flux tube is formed so as to minimize the total flux-tube length of the system for the low-lying state. For the low-lying 4Q system, there are two candidates for the flux-tube configuration according to the 4Q location. One is the connected flux-tube system where all quarks and antiquarks are connected with the single flux tube as shown in Fig. 3. The other is the disconnected flux tubes corresponding to a "two-meson" state as shown in Fig. 4. Note that the 4Q state of $((QQ)_{\bar{3}} - (\bar{Q}\bar{Q})_3)_1$ generally includes such a two-meson state of $(Q\bar{Q})_1(Q\bar{Q})_1$ as shown in the Appendix. For each case, we consider below the theoretical form of the tetraquark potential V_{4Q}.

1. OGE plus multi-Y Ansatz for the connected 4Q system

For the connected 4Q system, we propose the "OGE plus multi-Y Ansatz" as a theoretical form of V_{4Q} from the viewpoint of the flux-tube picture. This type of the flux-tube configuration is plausible when the distance between QQ and $\bar{Q}\bar{Q}$ is long enough compared with the size of these clusters. For such a system, all quarks and antiquarks are linked by the connected double-Y-shaped flux tube as
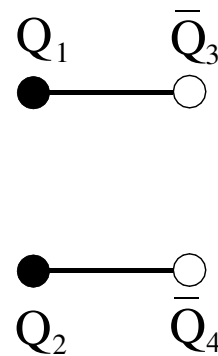
FIG. 2. The tetraquark $(QQ\text{-}\bar{Q}\bar{Q})$ state. The QQ $(\bar{Q}\bar{Q})$ cluster belongs to $\bar{3}$ (**3**) representation of the color SU(3).

FIG. 4. The disconnected tetraquark system, which corresponds to a "two-meson" state.

shown in Fig. 3, and the 4Q potential V_{4Q} is described by the OGE Coulomb plus multi-Y linear potential V_{c4Q} as

$$V_{4Q} = \frac{g^2}{4\pi} \sum_{i<j} \frac{T_i^a T_j^a}{|\mathbf{r}_i - \mathbf{r}_j|} + \sigma_{4Q} L_{\min} + C_{4Q}$$

$$= -A_{4Q}\left\{ \left(\frac{1}{r_{12}} + \frac{1}{r_{34}} \right) + \frac{1}{2}\left(\frac{1}{r_{13}} + \frac{1}{r_{14}} + \frac{1}{r_{23}} + \frac{1}{r_{24}} \right) \right\}$$

$$+ \sigma_{4Q} L_{\min} + C_{4Q} \equiv V_{c4Q} \qquad (5)$$

with $r_{ij} \equiv |\mathbf{r}_i - \mathbf{r}_j|$ and $L_{\min}$ being the minimal value of the total flux-tube length. Here, $\mathbf{r}_i$ denotes the location of the ith (anti)quark in Fig. 3.

The first term describes the Coulomb term due to the OGE process. Note that there appear two kinds of Coulomb coefficients $(A_{4Q}, \frac{1}{2}A_{4Q})$ in the 4Q system, while only one Coulomb coefficient, $A_{Q\bar{Q}}$ or A_{3Q}, appears in the $Q\bar{Q}$ or the 3Q system. In this definition, the Coulomb coefficient A_{4Q} is expected to satisfy $A_{4Q} \simeq \frac{1}{2}A_{Q\bar{Q}}$ as the OGE results. The brief derivation of the OGE Coulomb terms is shown in the Appendix.

The second term is the linear confinement term with the string tension σ_{4Q}, which is expected to satisfy $\sigma_{4Q} \simeq \sigma_{Q\bar{Q}} \simeq 0.89$ GeV/fm as the universality of the string tension. Similar to the 3Q and the 5Q systems, the Y-type junction appears in this case, and $L_{\min}$ is expressed by the length of the double-Y-shaped flux tube as shown in Fig. 3.

In the extreme case, e.g., $r_{12} = r_{34} \gg r_{13} = r_{24}$, the lowest connected 4Q system takes an X-shaped flux tube, although the energy of such system is larger than that of the two-meson state in most cases.

2. The two-meson Ansatz for the disconnected 4Q system

For the disconnected 4Q system corresponding to the two-meson state as shown in Fig. 4, we adopt the "two-meson Ansatz" for V_{4Q}. Such a flux-tube configuration is plausible when the nearest quark and antiquark pair is spatially close and the system can be regarded as the "two-meson state" rather than an inseparable 4Q state. For such a system as shown in Fig. 4, the total potential V_{4Q} for the 4Q system would be approximated to be the sum of two $Q\bar{Q}$ potentials in Eq. (1) as

$$V_{4Q} = V_{Q\bar{Q}}(r_{13}) + V_{Q\bar{Q}}(r_{24})$$

$$= -A_{Q\bar{Q}}\left(\frac{1}{r_{13}} + \frac{1}{r_{24}} \right) + \sigma_{Q\bar{Q}}(r_{13} + r_{24}) + 2C_{Q\bar{Q}}$$

$$\equiv V_{2Q\bar{Q}}, \qquad (6)$$

assuming that the intermeson force is subdominant.

C. The 4Q potential form and the flip-flop

For the lowest 4Q system, the 4Q potential V_{4Q} would be expressed with lower energy of the connected 4Q system or

the two-meson system,

$$V_{4Q} = \min(V_{c4Q}, V_{2Q\bar{Q}}). \qquad (7)$$

As a physical consequence of Eq. (7) based on the flux-tube picture, there can occur a physical transition between the connected 4Q state and the two-meson state according to the change of the 4Q location. This phenomenon occurs through the recombination of the flux tube and is called the flip-flop. (A popular usage of the flip-flop may be for the simple flux-tube recombination between two-meson states. We here use this term as the general flux-tube recombination.)

The flip-flop is important for the properties of 4Q states especially for the decay process into two mesons. In addition, the flux-tube recombination between two-meson states can be realized through the two successive flip-flops between the two-meson state and the connected 4Q state. Therefore, this type of the flip-flop is important also for the reaction mechanism between two mesons.

III. FORMALISM FOR THE 4Q POTENTIAL IN LATTICE QCD

In this section, we present the formalism to extract the static 4Q potential. Similar to the derivation of the $Q\bar{Q}$ potential from the Wilson loop, the 4Q potential V_{4Q} can be derived from the gauge-invariant 4Q Wilson loop W_{4Q} as shown in Fig. 5 [38,41,42].

The 4Q Wilson loop is defined by

$$W_{4Q} \equiv \frac{1}{3} \operatorname{tr}(\tilde{M}_1 \tilde{L}_{12} \tilde{M}_2 \tilde{R}_{12}). \qquad (8)$$

$\tilde{M}_i$, $\tilde{L}_i$, $\tilde{R}_i$ ($i = 1, 2$) are given by

$$\tilde{M}_i, \tilde{L}_i, \tilde{R}_i \equiv P \exp\left\{ ig \int_{M_i, L_i, R_i} dx^\mu A_\mu(x) \right\} \in \mathrm{SU}(3)_c. \qquad (9)$$

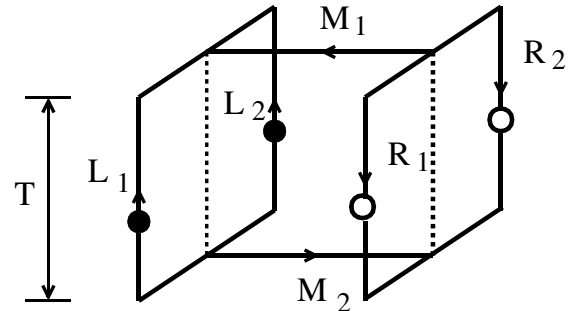Here, $\tilde{L}_{12}$ and $\tilde{R}_{12}$ are defined by

FIG. 5. The 4Q Wilson loop for the calculation of the 4Q potential V_{4Q}. The contours M_i ($i = 1, 2$) are linelike, and L_i, R_i ($i = 1, 2$) are staplelike. The 4Q gauge-invariant state is generated at $t = 0$ and is annihilated at $t = T$. The four quarks ($QQ\bar{Q}\bar{Q}$) are spatially fixed in $\mathbf{R}^3$ for $0 < t < T$.

$$\tilde{L}_{12}^{\,a'a} \equiv \frac{1}{2} \epsilon^{abc} \epsilon^{a'b'c'} L_1^{bb'} L_2^{cc'}, \qquad (10)$$

$$\tilde{R}_{12}^{\,a'a} \equiv \frac{1}{2} \epsilon^{abc} \epsilon^{a'b'c'} R_1^{bb'} R_2^{cc'}. \qquad (11)$$

The ground-state 4Q potential V_{4Q} is extracted as

$$V_{4Q} = -\lim_{T \to \infty} \frac{1}{T} \ln\langle W_{4Q}\rangle. \qquad (12)$$

In general, the 4Q Wilson loop $\langle W_{4Q}\rangle$ contains excited-state contributions and is expressed as

$$\langle W_{4Q}\rangle = \sum_{n=0}^{\infty} C_n e^{-V_n T}, \qquad (13)$$

where V_0 denotes the ground-state 4Q potential V_{4Q} and V_n ($n = 1, 2, 3, \ldots$) the nth excited-state potential. In principle, V_{4Q} can be obtained from the behavior of $\langle W_{4Q}\rangle$ at the large T region where the ground-state contribution becomes dominant. In the practical simulation, however, the accurate measurement of V_{4Q} is not easy for large T, since $\langle W_{4Q}\rangle$ decreases exponentially with T.

To extract the ground-state potential V_{4Q} in lattice QCD, we adopt the gauge-covariant smearing method [2–7] to enhance the ground-state component of the 4Q state in the 4Q Wilson loop. The smearing is known to be a powerful method for the accurate measurement of the Q-$\bar{Q}$ [2–4] and the 3Q potentials [5–7] and is expressed as the iterative replacement of the spatial link variables $U_i(s)$ ($i = 1, 2, 3$) by the obscured link variables $\bar{U}_i(s) \in \mathrm{SU}(3)_c$ which maximizes $\mathrm{Re}\,\mathrm{tr}\{\bar{U}_i^\dagger(s)V_i(s)\}$ with

$$V_i(s) \equiv \alpha U_i(s) + \sum_{j \neq i} \sum_{\pm} \{U_{\pm j}(s)U_i(s \pm \hat{j})U_{\pm j}^\dagger(s + \hat{i})\} \qquad (14)$$

with the simplified notation of $U_{-j} \equiv U_j^\dagger(s - \hat{j})$. We here adopt the smearing parameter $\alpha = 2.3$ and the iteration number $N_{\mathrm{smr}} = 30$, which enhance the ground-state component in the 4Q Wilson loop at $\beta = 6.0$ in most cases (see the next section).

IV. LATTICE QCD RESULTS FOR THE 4Q POTENTIAL

The lattice QCD simulations are performed with the standard plaquette action at $\beta = 6.0$ on the $16^3 \times 32$ lattice at the quenched level. The lattice spacing a is estimated as $a \simeq 0.104$ fm, which leads to the string tension $\sigma_{Q\bar{Q}} \simeq (427\ \mathrm{MeV})^2$ in the $Q\bar{Q}$ potential, using the numerical relation $\sigma_{Q\bar{Q}} \simeq 0.0506a^{-2}$ obtained from the fitting analysis on the on-axis data of the $Q\bar{Q}$ potential in lattice QCD at $\beta = 6.0$ [6,8]. The gauge configurations are taken every 500 sweeps after 5000 sweeps using the pseudo-heat-bath algorism. We use 300 configurations for the 4Q po-
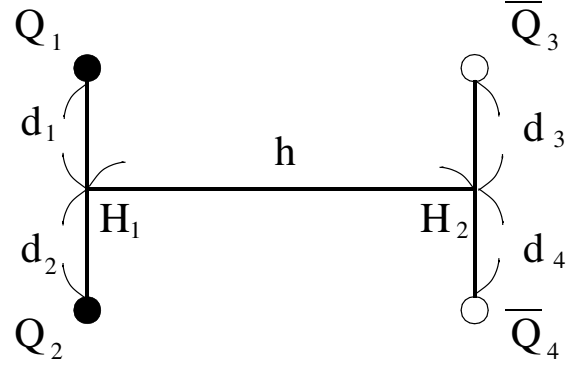
FIG. 6.   A planar configuration of the tetraquark system. $Q_1 Q_2$ is parallel to $\bar{Q}_3\bar{Q}_4$, and $H_1 H_2$ is perpendicular to $Q_1 Q_2$ and $\bar{Q}_3\bar{Q}_4$. We call the cases with $d_1 = d_2 = d_3 = d_4 \equiv d$ as "symmetric planar 4Q configurations."
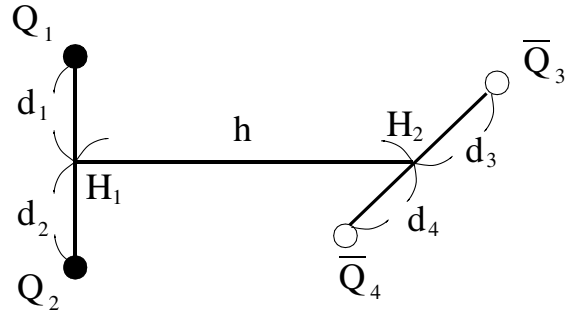
FIG. 7.   A twisted configuration of the tetraquark system. $Q_1 Q_2$ is perpendicular to $\bar{Q}_3\bar{Q}_4$, and $H_1 H_2$ is perpendicular to $Q_1 Q_2$ and $\bar{Q}_3\bar{Q}_4$. We call the cases with $d_1 = d_2 = d_3 = d_4 \equiv d$ as "symmetric twisted 4Q configurations."
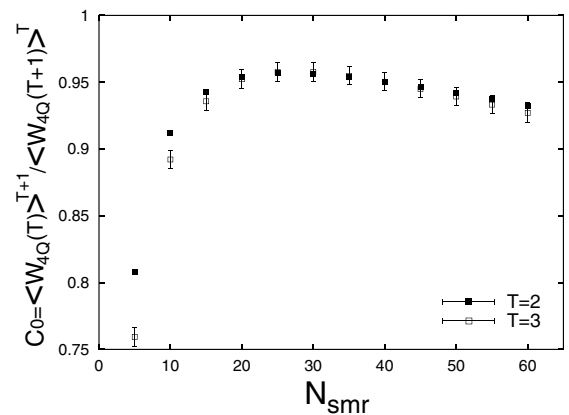
FIG. 8.   A typical example of the ground-state-overlap quantity $C_0 \equiv \langle W_{4Q}(T)\rangle^{T+1}/\langle W_{4Q}(T + 1)\rangle^T$ plotted against the iteration number N_{smr} at $\alpha = 2.3$ for the symmetric planar 4Q configuration with $(d, h) = (1, 5)$. C_0 takes a large value close to unity around $N_{\mathrm{smr}} = 30$.

tential simulation. For the estimation of the statistical error of the lattice data, we adopt the jackknife error estimate.

On the $16^3 \times 32$ lattice, we investigate the typical configuration of 4Q systems as shown in Figs. 6 and 7. In Fig. 6, the 4Q system has a planar structure. In Fig. 7, the 4Q system has a twisted (three-dimension) structure. In particular, we analyze in detail the symmetric planar and twisted 4Q configurations with $d_1 = d_2 = d_3 = d_4 \equiv d$, although more general asymmetric 4Q configurations with various (d_1, d_2, d_3, d_4) are also investigated.

For the 4Q configurations with $h \leq 8$, we identify 16^3 as the spatial size and 32 as the temporal one. On the other hand, the calculation for the large-size 4Q configurations with $h > 8$ is performed by identifying $16^2 \times 32$ as the

spatial size and 16 as the temporal one. In both cases, we use corresponding translational and rotational symmetries on lattices for the calculation of $\langle W_{4Q} \rangle$.

For these types of 4Q configurations, we construct the 4Q Wilson loop W_{4Q} with the junctions locating at H_1 and H_2, and calculate the 4Q potential V_{4Q} from $\langle W_{4Q} \rangle$ using the smearing method.

For the suitable choice of the smearing parameter α and the iteration number N_{smr} in Eq. (14), we perform some numerical tests with various values of α and N_{smr}, and finally adopt $\alpha = 2.3$ and $N_{\mathrm{smr}} = 30$, which are found to enhance the ground-state component in the 4Q Wilson loop at $\beta = 6.0$ in most cases. For the demonstration, we show in Fig. 8 a typical example of the ground-state-overlap

TABLE I. A part of the lattice QCD results of the 4Q potential V_{4Q} for the planar 4Q configuration as shown in Fig. 6 with $d_1 = d_2 = d_3 = d_4 \equiv d$. The symmetric planar 4Q systems are labeled by (d, h). We list also the ground-state overlap $\bar{C}$, the fit range of T, χ^2/N_{DF}, the minimal flux-tube length L_{min}^{c4Q} for the connected 4Q configuration, and the theoretical Ansätze. V_{c4Q}^{th} denotes the OGE Coulomb plus multi-Y Ansatz (5) with (A_{4Q}, σ_{4Q}) fixed to be (A_{3Q}, σ_{3Q}) in V_{3Q} in Ref. [6]. $V_{2Q\bar{Q}}^{\mathrm{th}}$ denotes the two-meson Ansatz (6) with $V_{Q\bar{Q}}$ in Ref. [6]. All the quantities are measured in the lattice unit at $\beta = 6.0$, i.e., $a \simeq 0.104$ fm.

(d, h)	V_{4Q}	$\bar{C}$	T_{min}-T_{max}	χ^2/N_{DF}	L_{min}^{c4Q}	V_{c4Q}^{th}	$V_{2Q\bar{Q}}^{\mathrm{th}}$
(1,1)	0.8590(45)	0.4970(135)	6-11	0.140	4.47	1.1293	0.8224
(1,2)	1.2124(31)	0.9049(111)	4-9	0.710	5.46	1.2560	1.2004
(1,3)	1.3218(17)	0.9572(48)	3-9	0.195	6.46	1.3352	1.3939
(1,4)	1.3938(11)	0.9627(19)	2-8	0.755	7.46	1.3999	1.5412
(1,5)	1.4531(13)	0.9556(22)	2-8	0.633	8.46	1.4579	1.6701
(1,6)	1.5051(33)	0.9354(95)	3-9	0.072	9.46	1.5123	1.7897
(1,7)	1.5644(19)	0.9434(32)	2-7	0.336	10.46	1.5643	1.9041
(1,8)	1.6184(20)	0.9375(36)	2-8	0.124	11.46	1.6150	2.0152
(1,9)	1.6706(22)	0.9295(35)	2-4	0.119	12.46	1.6646	2.1241
(1,10)	1.7269(28)	0.9286(48)	2-7	0.184	13.46	1.7136	2.2314
(1,11)	1.7774(30)	0.9177(48)	2-4	0.001	14.46	1.7620	2.3377
(1,12)	1.8234(37)	0.8983(62)	2-7	1.094	15.46	1.8100	2.4431
(1,13)	1.8797(44)	0.8979(74)	2-7	0.351	16.46	1.8577	2.5478
(1,14)	1.9285(49)	0.8838(78)	2-6	0.899	17.46	1.9052	2.6521
(1,15)	1.9787(55)	0.8722(91)	2-7	0.361	18.46	1.9525	2.7559
(1,16)	2.0365(62)	0.8741(101)	2-6	0.702	19.46	1.9996	2.8594
(2,1)	0.8263(46)	0.3324(93)	6-13	0.624	8.25	1.3992	0.8224
(2,2)	1.2633(183)	0.5646(514)	5-9	0.727	8.94	1.5022	1.2004
(2,3)	1.4592(111)	0.7457(328)	4-7	0.119	9.93	1.5734	1.3939
(2,4)	1.5950(17)	0.9223(29)	2-7	0.643	10.93	1.6340	1.5412
(2,5)	1.6619(21)	0.9286(36)	2-6	0.779	11.93	1.6896	1.6701
(2,6)	1.7215(23)	0.9285(41)	2-7	0.653	12.93	1.7426	1.7897
(2,7)	1.7791(29)	0.9283(51)	2-6	0.089	13.93	1.7938	1.9041
(2,8)	1.8279(31)	0.9121(54)	2-6	0.631	14.93	1.8439	2.0152
(2,9)	1.8827(34)	0.9101(57)	2-7	0.111	15.93	1.8932	2.1241
(2,10)	1.9366(38)	0.9049(64)	2-6	0.108	16.93	1.9419	2.2314
(2,11)	1.9917(45)	0.9026(73)	2-5	0.785	17.93	1.9902	2.3377
(2,12)	2.0419(49)	0.8911(82)	2-5	0.215	18.93	2.0381	2.4431
(2,13)	2.0954(55)	0.8856(90)	2-6	0.445	19.93	2.0857	2.5478
(2,14)	2.1387(61)	0.8619(101)	2-5	1.272	20.93	2.1331	2.6521
(2,15)	2.1990(67)	0.8683(111)	2-5	1.103	21.93	2.1804	2.7559
(2,16)	2.2482(78)	0.8567(122)	2-5	0.687	22.93	2.2274	2.8594

quantity

$$C_0 \equiv \langle W_{4Q}(T)\rangle^{T+1}/\langle W_{4Q}(T+1)\rangle^T \qquad (15)$$

plotted against the iteration number N_{smr} at $\alpha = 2.3$ for the symmetric planar 4Q configuration with $(d, h) = (1, 5)$. Here, the ground-state-overlap quantity C indicates the magnitude of the ground-state component [5,6] and is found to take a large value close to unity around $N_{smr} = 30$. (Note here that the enhancement of the ground-state component is the aim of the smearing, and hence any approximate optimization is applicable as long as the ground-state overlap is enough large.)

Because of the smearing, the ground-state component is largely enhanced in most cases, and therefore the 4Q Wilson loop $\langle W_{4Q}\rangle$ composed with the smeared link variable exhibits a single-exponential behavior as $\langle W_{4Q}\rangle \simeq e^{-V_{4Q}T}$ even for a small value of T. Then, for each 4Q configuration, we extract V_{4Q} from the least squares fit with the single-exponential form

$$\langle W_{4Q}\rangle = \bar{C}e^{-V_{4Q}T} \qquad (16)$$

in the range of $T_{min} \leq T \leq T_{max}$ listed in Tables I, II, III, IV, V, and VI. The prefactor $\bar{C}$ physically means the ground-state overlap, and $\bar{C} \simeq 1$ corresponds to the realization of the quasiground state. Here, we choose the fit range of T such that the stability of the "effective mass"

$$V(T) \equiv \ln\{\langle W_{4Q}(T)\rangle/\langle W_{4Q}(T+1)\rangle\} \qquad (17)$$

is observed in the range of $T_{min} \leq T \leq T_{max} - 1$.

To see how excited-state contamination is removed in this calculation, we show in Fig. 9 several effective-mass plots, $V(T)$ vs T, for planar and twisted 4Q configurations at small, intermediate, and large distances, respectively. Owing to the smearing, the effective mass $V(T)$ seems to be stable even for small T. To show the quality of the single-exponential fit for $\langle W_{4Q}\rangle$ as in Eq. (16), we list the chi square per degree of freedom, χ^2/N_{DF}, for each fit in

TABLE II. A part of the lattice QCD results of the 4Q potential V_{4Q} for the symmetric planar 4Q configuration labeled by (d, h). The notations are the same as in Table I.

(d, h)	V_{4Q}	$\bar{C}$	T_{min}-T_{max}	χ^2/N_{DF}	L_{min}^{c4Q}	V_{c4Q}^{th}	$V_{2Q\bar{Q}}^{th}$
(3,1)	0.8281(20)	0.3242(33)	5-12	0.502	12.17	1.6129	0.8224
(3,2)	1.2143(228)	0.3390(387)	5-9	0.237	12.65	1.7043	1.2004
(3,3)	1.5031(168)	0.5540(370)	4-7	2.112	13.42	1.7636	1.3939
(3,4)	1.6992(68)	0.7751(158)	3-7	0.654	14.39	1.8213	1.5412
(3,5)	1.8185(31)	0.8797(53)	2-6	0.446	15.39	1.8756	1.6701
(3,6)	1.8896(35)	0.8922(60)	2-6	0.299	16.39	1.9275	1.7897
(3,7)	1.9459(37)	0.8849(63)	2-4	1.708	17.39	1.9780	1.9041
(3,8)	2.0016(45)	0.8808(76)	2-5	0.933	18.39	2.0276	2.0152
(3,9)	2.0544(45)	0.8739(73)	2-4	0.003	19.39	2.0766	2.1241
(3,10)	2.1123(52)	0.8748(85)	2-6	0.116	20.39	2.1250	2.2314
(3,11)	2.1658(57)	0.8698(92)	2-7	0.241	21.39	2.1731	2.3377
(3,12)	2.2234(65)	0.8720(105)	2-5	0.373	22.39	2.2208	2.4431
(3,13)	2.2698(73)	0.8548(118)	2-5	0.168	23.39	2.2683	2.5478
(3,14)	2.3192(88)	0.8418(143)	2-5	0.417	24.39	2.3157	2.6521
(3,15)	2.3843(94)	0.8564(154)	2-6	0.653	25.39	2.3628	2.7559
(3,16)	2.4393(112)	0.8530(185)	2-5	0.469	26.39	2.4098	2.8594
(4,1)	0.8228(21)	0.3069(34)	5-12	0.586	16.12	1.8119	0.8224
(4,2)	1.2510(77)	0.3541(110)	4-9	0.528	16.49	1.8975	1.2004
(4,3)	1.4643(247)	0.3390(336)	4-7	0.247	17.09	1.9482	1.3939
(4,4)	1.7452(112)	0.5783(194)	3-7	0.910	17.89	1.9972	1.5412
(4,5)	1.9147(159)	0.7137(337)	3-5	1.694	18.86	2.0493	1.6701
(4,6)	2.0168(230)	0.7591(518)	3-7	0.425	19.86	2.1007	1.7897
(4,7)	2.1167(49)	0.8435(84)	2-4	0.041	20.86	2.1507	1.9041
(4,8)	2.1712(56)	0.8341(89)	2-4	0.436	21.86	2.2000	2.0152
(4,9)	2.2444(62)	0.8611(102)	2-6	0.363	22.86	2.2486	2.1241
(4,10)	2.2970(84)	0.8505(138)	2-5	1.626	23.86	2.2968	2.2314
(4,11)	2.3430(84)	0.8332(133)	2-6	0.514	24.86	2.3447	2.3377
(4,12)	2.3976(96)	0.8309(149)	2-5	0.544	25.86	2.3923	2.4431
(4,13)	2.4503(109)	0.8225(168)	2-4	0.030	26.86	2.4397	2.5478
(4,14)	2.5043(123)	0.8178(194)	2-4	0.070	27.86	2.4869	2.6521
(4,16)	2.6037(177)	0.7952(276)	2-4	2.015	29.86	2.5809	2.8594

Tables I, II, III, IV, V, and VI. For most cases, χ^2/N_{DF} takes a small value less than unity, and the fitting seems to be plausible. [We note that the errors listed in Tables I, II, III, IV, V, and VI are statistical ones, and there are some systematical errors in the lattice QCD calculation. For instance, when $T_{min} = 2$ is adopted for large 4Q systems as $(d, h) = (3, 16)$, the systematical error originating from the fit-range choice seems to be several times larger than the statistical error.]

In this way, we calculate the tetraquark potential V_{4Q} for various 4Q systems, i.e., planar, twisted, asymmetric, and large-size 4Q configurations, respectively. We summarize in Tables I, II, III, IV, V, and VI the lattice QCD results for V_{4Q} together with the ground-state overlap $\bar{C}$, the fit range of T, χ^2/N_{DF}, the minimal flux-tube length L_{min}^{c4Q} for the connected 4Q configuration, and the theoretical Ansätze V_{c4Q}^{th} and $V_{2Q\bar{Q}}^{th}$ presented in Sec. II.

(1) Tables I and II show V_{4Q} for the symmetric planar 4Q configurations as shown in Fig. 6 with $d_1 = d_2 = d_3 = d_4 \equiv d$. V_{4Q} is shown in terms of d and h.

(2) Tables III and IV show V_{4Q} for the symmetric twisted 4Q configurations as shown in Fig. 7 with $d_1 = d_2 = d_3 = d_4 \equiv d$. V_{4Q} is shown in terms of d and h.

(3) Table V shows V_{4Q} for the asymmetric planar 4Q configurations as shown in Fig. 6 with various (d_1, d_2, d_3, d_4) for $h = 8$.

(4) Table VI shows V_{4Q} for the asymmetric twisted 4Q configurations as shown in Fig. 7 with various (d_1, d_2, d_3, d_4) for $h = 8$.

Thus, we obtain the tetraquark potential V_{4Q} for about 200 different patterns of 4Q systems.

TABLE III. A part of the lattice QCD results of the 4Q potential V_{4Q} for the twisted 4Q configuration as shown in Fig. 7 with $d_1 = d_2 = d_3 = d_4 \equiv d$. The symmetric twisted 4Q systems are labeled by (d, h). The notations are the same as in Table I.

(d, h)	V_{4Q}	$\bar{C}$	T_{min}-T_{max}	χ^2/N_{DF}	L_{min}^{c4Q}	V_{c4Q}^{th}	$V_{2Q\bar{Q}}^{th}$
(1,1)	1.1779(06)	0.9695(11)	2-8	0.695	4.47	1.1693	1.1305
(1,2)	1.2577(06)	0.9687(11)	2-5	0.009	5.46	1.2611	1.2967
(1,3)	1.3311(08)	0.9676(15)	2-8	0.465	6.46	1.3362	1.4435
(1,4)	1.3960(11)	0.9642(20)	2-6	0.676	7.46	1.4002	1.5737
(1,5)	1.4532(13)	0.9546(23)	2-8	0.546	8.46	1.4580	1.6941
(1,6)	1.5100(35)	0.9497(99)	3-8	0.221	9.46	1.5123	1.8088
(1,7)	1.5661(18)	0.9472(32)	2-7	0.305	10.46	1.5644	1.9200
(1,8)	1.6177(21)	0.9357(37)	2-7	0.311	11.46	1.6150	2.0288
(1,9)	1.6712(24)	0.9300(41)	2-7	0.416	12.46	1.6646	2.1360
(1,10)	1.7144(68)	0.8956(180)	3-5	0.006	13.46	1.7136	2.2421
(1,11)	1.7751(32)	0.9134(53)	2-5	0.890	14.46	1.7620	2.3472
(1,12)	1.8302(38)	0.9109(65)	2-6	0.039	15.46	1.8100	2.4518
(1,13)	1.8778(45)	0.8946(76)	2-6	0.689	16.46	1.8577	2.5558
(1,14)	1.9306(49)	0.8879(79)	2-6	0.543	17.46	1.9052	2.6595
(1,15)	1.9860(56)	0.8856(90)	2-6	0.649	18.46	1.9525	2.7628
(1,16)	2.0378(62)	0.8771(99)	2-5	0.100	19.46	1.9996	2.8658
(2,1)	1.4571(27)	0.9244(72)	3-6	0.130	8.25	1.4778	1.3939
(2,2)	1.5027(32)	0.9296(89)	3-8	0.131	8.94	1.5221	1.4656
(2,3)	1.5613(14)	0.9445(24)	2-4	0.033	9.93	1.5800	1.5578
(2,4)	1.6152(18)	0.9388(31)	2-7	0.339	10.93	1.6365	1.6576
(2,5)	1.6713(18)	0.9367(31)	2-4	0.499	11.93	1.6907	1.7598
(2,6)	1.7249(22)	0.9305(38)	2-4	0.266	12.93	1.7431	1.8626
(2,7)	1.7780(27)	0.9241(47)	2-7	0.439	13.93	1.7941	1.9655
(2,8)	1.8305(29)	0.9162(50)	2-4	0.044	14.93	1.8441	2.0683
(2,9)	1.8752(35)	0.8945(58)	2-6	2.241	15.93	1.8933	2.1708
(2,10)	1.9335(40)	0.8985(68)	2-6	0.989	16.93	1.9420	2.2732
(2,11)	1.9882(45)	0.8961(74)	2-6	0.776	17.93	1.9902	2.3755
(2,12)	2.0295(51)	0.8681(82)	2-5	1.912	18.93	2.0381	2.4776
(2,13)	2.0933(56)	0.8818(92)	2-4	0.042	19.93	2.0857	2.5796
(2,14)	2.1470(62)	0.8768(102)	2-5	0.015	20.93	2.1331	2.6815
(2,15)	2.1910(70)	0.8552(115)	2-7	0.874	21.93	2.1804	2.7833
(2,16)	2.2315(76)	0.8272(119)	2-5	0.884	22.93	2.2274	2.8850

TABLE IV.   A part of the lattice QCD results of the 4Q potential V_{4Q} for the symmetric twisted 4Q configuration labeled by (d, h). The notations are the same as in Table I.

(d, h)	V_{4Q}	$\bar{C}$	$T_{\min}$-$T_{\max}$	χ^2/N_{DF}	$L_{\min}^{c4Q}$	V_{c4Q}^{th}	$V_{2Q\bar{Q}}^{th}$
(3,1)	1.6641(20)	0.9086(34)	2-8	1.052	12.17	1.7093	1.5889
(3,2)	1.6980(21)	0.9095(35)	2-4	0.227	12.65	1.7359	1.6314
(3,3)	1.7444(25)	0.9098(43)	2-6	0.649	13.42	1.7769	1.6941
(3,4)	1.7960(26)	0.9085(46)	2-5	0.278	14.39	1.8275	1.7700
(3,5)	1.8473(31)	0.9017(53)	2-5	0.747	15.39	1.8787	1.8540
(3,6)	1.9015(36)	0.8995(60)	2-6	0.151	16.39	1.9292	1.9431
(3,7)	1.9563(39)	0.8969(66)	2-6	0.334	17.39	1.9790	2.0355
(3,8)	2.0077(46)	0.8888(75)	2-6	0.216	18.39	2.0282	2.1301
(3,9)	2.0609(47)	0.8838(77)	2-6	0.067	19.39	2.0769	2.2261
(3,10)	2.1146(52)	0.8787(86)	2-5	0.121	20.39	2.1252	2.3232
(3,11)	2.1695(56)	0.8763(91)	2-4	0.104	21.39	2.1732	2.4210
(3,12)	2.2284(65)	0.8805(109)	2-6	0.053	22.39	2.2209	2.5194
(3,13)	2.2684(69)	0.8513(112)	2-6	0.676	23.39	2.2684	2.6182
(3,14)	2.3303(82)	0.8597(133)	2-4	0.373	24.39	2.3157	2.7174
(3,15)	2.3725(96)	0.8357(151)	2-5	0.631	25.39	2.3629	2.8168
(3,16)	2.4051(112)	0.7968(168)	2-6	0.378	26.39	2.4099	2.9165
(4,1)	1.8453(33)	0.8666(56)	2-6	0.389	16.12	1.9179	1.7598
(4,2)	1.8396(124)	0.7745(285)	3-6	1.225	16.49	1.9368	1.7897
(4,3)	1.8832(135)	0.7758(315)	3-6	1.204	17.09	1.9671	1.8363
(4,4)	1.9745(44)	0.8706(71)	2-4	0.193	17.89	2.0072	1.8960
(4,5)	2.0271(47)	0.8670(79)	2-6	0.321	18.86	2.0549	1.9655
(4,6)	2.0749(52)	0.8536(85)	2-5	0.226	19.86	2.1040	2.0422
(4,7)	2.1306(52)	0.8522(86)	2-4	0.543	20.86	2.1528	2.1241
(4,8)	2.1932(66)	0.8640(108)	2-6	0.250	21.86	2.2012	2.2099
(4,9)	2.2409(62)	0.8510(101)	2-5	0.801	22.86	2.2494	2.2985
(4,10)	2.2867(66)	0.8331(107)	2-4	0.060	23.86	2.2973	2.3893
(4,11)	2.3324(87)	0.8152(135)	2-4	0.680	24.86	2.3450	2.4818
(4,12)	2.3951(107)	0.8247(166)	2-5	0.199	25.86	2.3925	2.5756
(4,13)	2.4477(110)	0.8173(174)	2-6	2.138	26.86	2.4398	2.6705
(4,14)	2.4910(128)	0.7958(196)	2-5	0.053	27.86	2.4870	2.7662
(4,15)	2.5625(154)	0.8210(238)	2-6	0.904	28.86	2.5341	2.8626
(4,16)	2.5995(155)	0.7897(238)	2-5	0.099	29.86	2.5810	2.9596

V. DISCUSSIONS

A. Comparison with theoretical Ansätze

In this section, we compare the lattice QCD results of the 4Q potential V_{4Q} with the theoretical Ansätze presented in Sec. II, i.e., the OGE plus multi-Y Ansatz (5) and the two-meson Ansatz (6).

For the OGE plus multi-Y Ansatz (5), we set the parameters (A_{4Q}, σ_{4Q}) to be (A_{3Q}, σ_{3Q}) in the 3Q potential V_{3Q} in Ref. [6], i.e., $A_{4Q} = A_{3Q} \simeq 0.1366$, $\sigma_{4Q} = \sigma_{3Q} \simeq 0.0460a^{-2}$. Note that there are no adjustable parameters except for an irrelevant constant $C_{4Q} \simeq 1.2579a^{-1}$.

For the two-meson Ansatz (6), we adopt the lattice result for the $Q\bar{Q}$ potential $V_{Q\bar{Q}}$ in Ref. [6], i.e., $A_{Q\bar{Q}} \simeq 0.2768$, $\sigma_{Q\bar{Q}} \simeq 0.0506a^{-2}$, $C_{Q\bar{Q}} \simeq 0.6374a^{-1}$. Then, there are no adjustable parameters also for the two-meson Ansatz.

We demonstrate the two Ansätze for the symmetric planar 4Q configurations as shown in Fig. 6 with $d_1 =$

$d_2 = d_3 = d_4 \equiv d$. In this case, the OGE Coulomb plus multi-Y Ansatz for the connected 4Q system reads

$$V_{c4Q}(d, h) = -A_{4Q}\left(\frac{1}{d} + \frac{1}{h} + \frac{1}{\sqrt{h^2 + 4d^2}}\right) + \sigma_{4Q}L_{\min} + C_{4Q}. \tag{18}$$

In the case of $h \geq \frac{2}{\sqrt{3}}d$, the lowest connected 4Q system takes the double-Y-shaped flux tube, and the minimal value of the total flux-tube length is expressed as

$$L_{\min} = h + 2\sqrt{3}d. \tag{19}$$

In the case of $h \leq \frac{2}{\sqrt{3}}d$, the lowest connected 4Q system takes the X-shaped flux tube with $L_{\min} = 2\sqrt{h^2 + 4d^2}$, although it must be unstable against the decay into two mesons. On the other hand, the two-meson Ansatz reads

TABLE V. Lattice QCD results for the 4Q potential V_{4Q} for the asymmetric planar 4Q configuration as shown in Fig. 6 with various (d_1, d_2, d_3, d_4) for $h = 8$. The notations are the same as in Table I.

(d_1, d_2, d_3, d_4)	V_{4Q}	$\bar{C}$	T_{min}-T_{max}	χ^2/N_{DF}	L^{c4Q}_{min}	V^{th}_{c4Q}	$V^{th}_{2Q\bar{Q}}$
(0,1,0,1)	1.4227(18)	0.9368(31)	2-10	0.610	9.73	1.3983	2.0152
(0,1,1,0)	1.4243(17)	0.9377(29)	2-10	0.265	9.78	1.4008	2.0220
(0,1,1,1)	1.5215(19)	0.9385(34)	2-8	0.544	10.61	1.5073	2.0186
(0,1,2,0)	1.5170(39)	0.9054(103)	3-7	0.424	10.70	1.5118	2.0321
(0,1,1,2)	1.5689(43)	0.8991(115)	3-8	0.596	11.46	1.5697	2.0220
(0,1,2,1)	1.5830(21)	0.9353(36)	2-7	0.155	11.51	1.5718	2.0287
(0,1,3,0)	1.5926(21)	0.9289(36)	2-7	0.086	11.64	1.5781	2.0483
(0,2,1,1)	1.6211(21)	0.9300(38)	2-7	0.388	11.51	1.6171	2.0220
(0,2,2,0)	1.6301(22)	0.9310(40)	2-7	0.199	11.64	1.6234	2.0422
(0,1,1,3)	1.6281(22)	0.9200(38)	2-8	0.687	12.34	1.6219	2.0321
(0,1,2,2)	1.6231(49)	0.9144(132)	3-8	0.221	12.34	1.6219	2.0321
(0,1,3,1)	1.6326(23)	0.9253(40)	2-7	0.758	12.42	1.6258	2.0449
(0,2,1,2)	1.6809(22)	0.9262(39)	2-6	0.779	12.34	1.6784	2.0186
(0,2,2,1)	1.6834(23)	0.9273(42)	2-8	0.762	12.42	1.6824	2.0321
(0,2,3,0)	1.6934(23)	0.9208(39)	2-5	0.470	12.58	1.6902	2.0584
(1,1,1,2)	1.6784(23)	0.9324(41)	2-7	0.510	12.34	1.6784	2.0186
(0,1,2,3)	1.6668(61)	0.9034(165)	3-6	0.309	13.20	1.6687	2.0422
(0,1,3,2)	1.6732(25)	0.9199(45)	2-6	0.502	13.23	1.6705	2.0483
(0,2,1,3)	1.7270(25)	0.9125(45)	2-6	0.683	13.20	1.7296	2.0220
(0,2,3,1)	1.7349(25)	0.9210(43)	2-7	0.323	13.35	1.7370	2.0483
(0,3,1,2)	1.7441(26)	0.9177(47)	2-7	0.369	13.23	1.7426	2.0220
(0,3,2,1)	1.7473(26)	0.9191(46)	2-7	0.503	13.35	1.7482	2.0422
(0,3,3,0)	1.7604(25)	0.9172(45)	2-7	0.166	13.53	1.7573	2.0747
(1,1,1,3)	1.7295(26)	0.9259(45)	2-7	0.880	13.23	1.7314	2.0287
(1,1,2,2)	1.7218(24)	0.9221(45)	2-6	0.307	13.20	1.7296	2.0220
(1,2,1,2)	1.7398(24)	0.9311(44)	2-6	0.254	13.20	1.7408	2.0152
(1,2,2,1)	1.7299(66)	0.9013(176)	3-9	0.298	13.23	1.7426	2.0220
(0,1,3,3)	1.7159(29)	0.9127(49)	2-6	0.559	14.07	1.7142	2.0584
(0,2,3,2)	1.7754(29)	0.9167(49)	2-9	0.893	14.14	1.7807	2.0449
(0,3,3,1)	1.8006(28)	0.9162(49)	2-6	1.013	14.28	1.8033	2.0584
(1,1,2,3)	1.7687(27)	0.9179(47)	2-9	0.558	14.07	1.7772	2.0321
(1,2,2,2)	1.7866(27)	0.9268(49)	2-6	0.192	14.07	1.7928	2.0186
(1,2,3,1)	1.7900(28)	0.9208(49)	2-6	0.436	14.14	1.7963	2.0321
(1,2,2,3)	1.8273(31)	0.9109(55)	2-6	0.881	14.93	1.8395	2.0220
(1,2,3,2)	1.8311(30)	0.9170(54)	2-7	0.284	14.96	1.8412	2.0287
(1,3,3,1)	1.8437(32)	0.9191(57)	2-6	0.449	15.06	1.8506	2.0422
(1,3,3,2)	1.8845(35)	0.9154(59)	2-6	0.173	15.87	1.8946	2.0321
(2,2,2,3)	1.8774(34)	0.9131(60)	2-7	0.197	15.80	1.8914	2.0186
(2,3,2,3)	1.9213(37)	0.9050(63)	2-6	0.030	16.66	1.9380	2.0152
(2,3,3,3)	1.9648(39)	0.8987(65)	2-6	0.603	17.53	1.9832	2.0186

$$V_{2Q\bar{Q}}(h) = 2 \times V_{Q\bar{Q}}(h), \qquad (20)$$

which is independent of d.

We show in Fig. 10(a) the lattice QCD results of the 4Q potential V_{4Q} for symmetric planar 4Q configurations [38,41,42] with $d = 1 - 4$. The symbols denote lattice QCD results. The curves describe the theoretical form: the solid curve denotes the OGE plus multi-Y Ansatz (5), and the dash-dotted curve the two-meson Ansatz (6).

For the large value of h compared with d, the lattice data seem to coincide with the OGE Coulomb plus multi-Y Ansatz [38,41]. On the other hand, for small h, the lattice data tend to agree with the two-meson Ansatz and seem independent of d [38,41]. These tendencies were also observed in a recent lattice work by another group [42]. This would correspond to the transition from the connected 4Q state into the two-meson state as h decreases, as will be discussed in the next subsection.

TABLE VI. Lattice QCD results for the 4Q potential V_{4Q} for the asymmetric twisted 4Q configuration as shown in Fig. 7 with various (d_1, d_2, d_3, d_4) for $h = 8$. The notations are the same as in Table I.

(d_1, d_2, d_3, d_4)	V_{4Q}	$\bar{C}$	$T_{\min}$-$T_{\max}$	χ^2/N_{DF}	$L_{\min}^{c4Q}$	V_{c4Q}^{th}	$V_{2Q\bar{Q}}^{\mathrm{th}}$
(0,1,0,1)	1.4179(34)	0.9197(92)	3-8	0.857	9.76	1.3997	2.0220
(0,1,1,1)	1.5239(18)	0.9435(34)	2-10	0.590	10.61	1.5074	2.0254
(0,1,0,2)	1.5152(129)	0.8961(453)	4-9	0.173	10.66	1.5100	2.0320
(0,1,1,2)	1.5819(47)	0.9340(132)	3-7	0.262	11.49	1.5709	2.0354
(0,1,0,3)	1.5896(21)	0.9257(37)	2-9	0.525	11.58	1.5756	2.0481
(0,2,1,1)	1.6248(20)	0.9373(36)	2-5	0.889	11.52	1.6176	2.0354
(0,2,0,2)	1.6259(22)	0.9263(38)	2-7	0.367	11.57	1.6202	2.0417
(0,1,1,3)	1.6279(53)	0.9144(143)	3-7	0.538	12.39	1.6241	2.0515
(0,1,2,2)	1.6252(50)	0.9204(140)	3-9	0.070	12.34	1.6219	2.0455
(0,2,1,2)	1.6813(24)	0.9250(42)	2-8	0.770	12.39	1.6811	2.0452
(0,2,0,3)	1.6923(23)	0.9233(38)	2-7	0.545	12.49	1.6858	2.0575
(1,1,1,2)	1.6790(22)	0.9334(39)	2-7	0.652	12.34	1.6785	2.0388
(0,1,2,3)	1.6724(24)	0.9192(43)	2-8	0.221	13.22	1.6696	2.0616
(0,2,1,3)	1.7335(25)	0.9213(45)	2-7	0.040	13.29	1.7343	2.0609
(0,3,1,2)	1.7462(25)	0.9187(45)	2-7	0.323	13.31	1.7467	2.0609
(0,3,0,3)	1.7567(27)	0.9166(47)	2-6	0.557	13.41	1.7514	2.0726
(1,1,1,3)	1.7293(25)	0.9252(45)	2-7	0.392	13.24	1.7317	2.0549
(1,1,2,2)	1.7220(24)	0.9222(45)	2-6	0.420	13.20	1.7296	2.0488
(1,2,1,2)	1.7388(27)	0.9280(46)	2-6	0.721	13.22	1.7420	2.0485
(0,1,3,3)	1.7198(27)	0.9199(47)	2-8	0.746	14.08	1.7141	2.0778
(0,2,2,3)	1.7734(28)	0.9138(49)	2-7	0.497	14.12	1.7798	2.0710
(0,3,1,3)	1.7979(28)	0.9145(49)	2-6	0.096	14.21	1.7999	2.0761
(1,1,2,3)	1.7687(29)	0.9174(53)	2-8	0.832	14.07	1.7772	2.0649
(1,2,2,2)	1.7840(28)	0.9210(49)	2-7	0.820	14.07	1.7930	2.0585
(1,2,1,3)	1.7890(30)	0.9201(51)	2-7	1.063	14.12	1.7952	2.0643
(1,2,2,3)	1.8312(30)	0.9169(53)	2-6	0.095	14.95	1.8407	2.0743
(1,3,1,3)	1.8393(31)	0.9128(54)	2-7	0.474	15.02	1.8484	2.0794
(1,3,2,3)	1.8853(34)	0.9164(58)	2-6	1.208	15.85	1.8939	2.0894
(2,2,2,3)	1.8807(33)	0.9180(55)	2-4	0.032	15.80	1.8917	2.0840
(2,3,2,3)	1.9171(36)	0.8943(64)	2-5	0.564	16.68	1.9394	2.0992
(2,3,3,3)	1.9653(40)	0.8968(69)	2-6	0.128	17.54	1.9838	2.1149

Here, we comment on the transition in terms of the ground-state overlap $\bar{C}$ listed in Table I. For large h, the ground-state overlap $\bar{C}$ is almost unity, which implies the realization of the quasiground state in the present calculation with the smeared 4Q Wilson loop based on the connected 4Q configuration. For small h, however, $\bar{C}$ tends to be small, and hence, for accurate measurements, we have to take relatively large values of T as the fit range. This would indicate that the ground-state configuration is largely different from the connected 4Q configuration for small h. (In other words, it may be nontrivial to obtain the result indicating the two-meson state for small h from the 4Q Wilson loop based on the connected 4Q configuration.)

Next, we investigate the twisted 4Q configuration [38,41] as shown in Fig. 7. We show in Fig. 10(b) the lattice QCD results of the 4Q potential for symmetric twisted 4Q configurations with $d = 1 - 4$. The symbols denote lattice QCD results for each d, and the curves

describe the theoretical form of the OGE plus multi-Y Ansatz.

The lattice data seem to agree with the OGE plus multi-Y Ansatz in the wide region of h [38,41]. In the twisted 4Q configuration, the distance between the nearest quark and antiquark cannot take a smaller value than the "interdiquark distance" h, and therefore V_{c4Q} is smaller than $V_{2Q\bar{Q}}$ in most cases except for extreme configurations as $d > h$ [see Fig. 10(b)]. Then, different from the planar case, it is not easy to make the transition from the connected 4Q state into the two-meson state for the twisted case. Also from the lattice data, the ground-state overlap $\bar{C}$ is found to be almost unity for all twisted 4Q configurations, which indicates that the ground state resembles a connected 4Q state. In other words, the twisted 4Q configuration seems to be rather stable against the transition into the two $Q\bar{Q}$ mesons, which may indicate a stability of the "twisted structure" or the "tetrahedral structure" of the 4Q system.
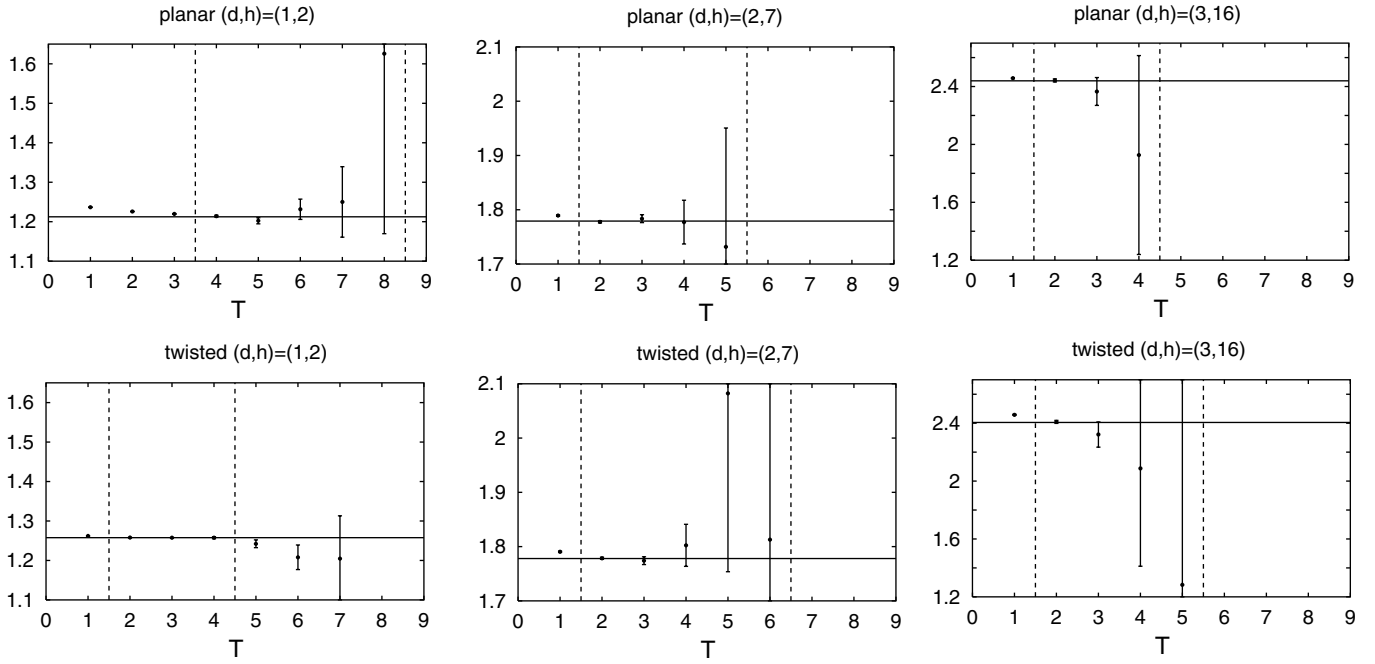
FIG. 9. The effective-mass plots, $V(T)$ vs T, for several 4Q configurations at small, intermediate, and large distances: the symmetric planar and twisted 4Q configurations with $(d, h) = (1, 2)$, $(d, h) = (2, 7)$, and $(d, h) = (3, 16)$. The fit range of $T_{\min} \leq T \leq T_{\max} - 1$, which is regarded as the plateau region, is indicated by the vertical dashed lines. The solid horizontal lines denote the final fit of V_{4Q} from the least square fit with the single-exponential form.

We also investigate more general asymmetric 4Q configurations with various (d_1, d_2, d_3, d_4) for both planar and twisted cases, as shown in Tables V and VI. Also for the asymmetric planar and twisted 4Q configurations, V_{4Q} seems to be well described with the OGE plus multi-Y Ansatz in the case of $h > \frac{2}{\sqrt{3}} d_i$ ($i = 1, 2, 3, 4$). Note here that some 4Q configurations are physically equivalent, e.g., the planar cases with $(d_1, d_2, d_3, d_4) = (1, 1, 1, 2)$ and $(0,2,1,2)$, although the corresponding smeared 4Q Wilson loops are different. For such cases, the lattice QCD results are found to be almost the same. In fact, the extracted

lattice results are almost independent of the way the 4Q Wilson loop is constructed, as long as the spatial locations of the static four quarks are the same. This indicates that the ground-state contribution is properly extracted in the present calculation.

As the conclusion, the OGE plus multi-Y Ansatz well describes the 4Q potential V_{4Q}, when QQ and $\bar{Q}\bar{Q}$ are well separated, e.g., the interdiquark distance h is large in comparison with the "diquark size" d. On the other hand, when the nearest quark and antiquark pair is spatially close, the system is described as a two-meson state.
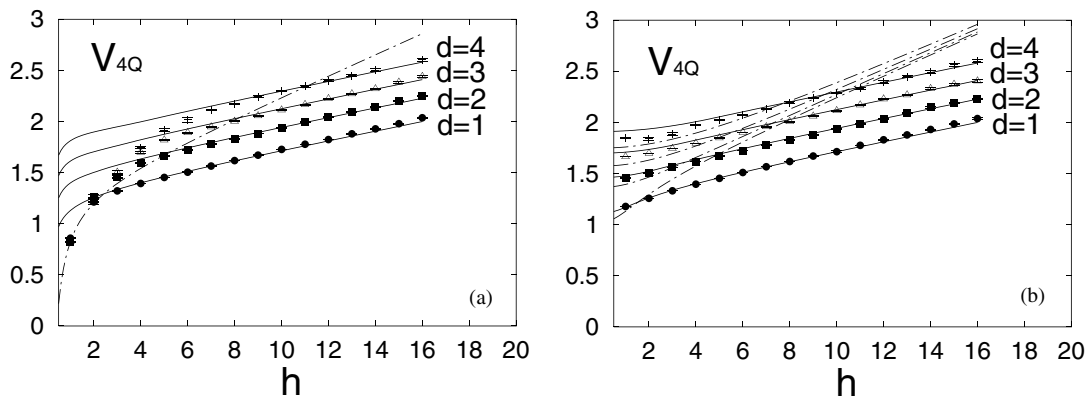

FIG. 10. The 4Q potential V_{4Q} (a) for symmetric planar 4Q configurations as shown in Fig. 6; (b) for symmetric twisted 4Q configurations as shown in Fig. 7. The symbols denote the lattice QCD results. The curves describe the theoretical form: the solid curves denote the OGE plus multi-Y Ansatz, and the dash-dotted curves the two-meson Ansatz.

Together with the previous studies [5,6,36–41] for the interquark potentials in lattice QCD, we have found the universality of the string tension as

$$\sigma_{Q\bar{Q}} \simeq \sigma_{3Q} \simeq \sigma_{4Q} \simeq \sigma_{5Q} \simeq (420 \text{ MeV})^2, \quad (21)$$

and the OGE result for the Coulomb coefficient as

$$A_{Q\bar{Q}} \simeq 2A_{3Q} \simeq 2A_{4Q} \simeq 2A_{5Q} \simeq 0.27. \quad (22)$$

In particular, these lattice QCD studies [36–41] indicate a fairly good agreement among σ_{3Q}, σ_{4Q}, and σ_{5Q}, which seem to be slightly smaller than $\sigma_{Q\bar{Q}}$. (As an interesting possibility, the numerical similarity among σ_{3Q}, σ_{4Q}, and σ_{5Q} may reflect the similar structure of the Y-type flux tube in the multiquark systems.) The universality of the string tension observed in our lattice QCD studies [5,6,36–41] seems to be consistent with the hypothetical flux-tube picture [49–56] or the strong-coupling expansion scheme [50,51], although strong-coupling QCD does not have a continuum limit and is far from real QCD. As for the irrelevant constant, $C_{Q\bar{Q}}$, C_{3Q}, C_{4Q}, and C_{5Q} are nonscaling unphysical quantities appearing in the lattice regularization, and we find an approximate relation as

$$\frac{C_{Q\bar{Q}}}{2} \simeq \frac{C_{3Q}}{3} \simeq \frac{C_{4Q}}{4} \simeq \frac{C_{5Q}}{5} \simeq 0.32a^{-1} \quad (23)$$

in lattice QCD [5,6,36–41].

B. The quark confinement force in 4Q systems

While the short-distance OGE Coulomb force can be understood with perturbative QCD, the long-distance confinement force is a typical nonperturbative quantity and highly nontrivial particularly for multiquark systems. To specify the long-distance property of V_{4Q} is important to clarify the confinement mechanism from a wide viewpoint

including multiquarks, and it also leads to a proper quark-model Hamiltonian to describe multiquark systems. Therefore, we perform a further analysis for the long-distance force in 4Q systems.

To clarify the long-distance force in the 4Q system, we plot V_{4Q} against $L_{\min}^{c4Q}$ for planar and twisted 4Q configurations in Figs. 11(a) and 11(b), respectively. Here, $L_{\min}^{c4Q}$ denotes the minimal flux-tube length for the connected 4Q system. In both planar and twisted cases, for large $L_{\min}^{c4Q}$, V_{4Q} approaches a linearly arising function of $L_{\min}^{c4Q}$.

To single out the long-distance confinement force, we consider the 4Q potential subtracted by the Coulomb part. Here, we subtract the OGE Coulomb part V_{c4Q}^{Coul} of V_{c4Q} in Eq. (5) for the connected 4Q system, with the Coulomb coefficient A_{4Q} fixed to be A_{3Q} in the 3Q potential V_{3Q} in Ref. [6]. We plot $V_{4Q} - V_{c4Q}^{\text{Coul}}$ against $L_{\min}^{c4Q}$ for planar and twisted 4Q configurations in Figs. 12(a) and 12(b), respectively. For the planar 4Q system, $V_{4Q} - V_{c4Q}^{\text{Coul}}$ approaches $\sigma_{4Q}L_{\min}^{c4Q} + C_{4Q}$ except for a small h region, where the flip-flop into a two-meson state can take place. For the twisted 4Q system, we observe remarkable agreement between the lattice QCD data of $V_{4Q} - V_{c4Q}^{\text{Coul}}$ and $\sigma_{4Q}L_{\min}^{c4Q} + C_{4Q}$ for the wide region of $L_{\min}$, which corresponds to the fact that the flip-flop into the two-meson state does not occur in most twisted 4Q configurations.

Thus, the confinement potential in the 4Q system as shown in Fig. 2 is proportional to $L_{\min}$, which indicates that the quark confinement force is genuinely 4-body and the flux tube is multi-Y-shaped.

C. The flip-flop, the level crossing, and absence of the color van der Waals force

Finally, we investigate the flip-flop between the connected 4Q state and the two-meson state. Since the flux
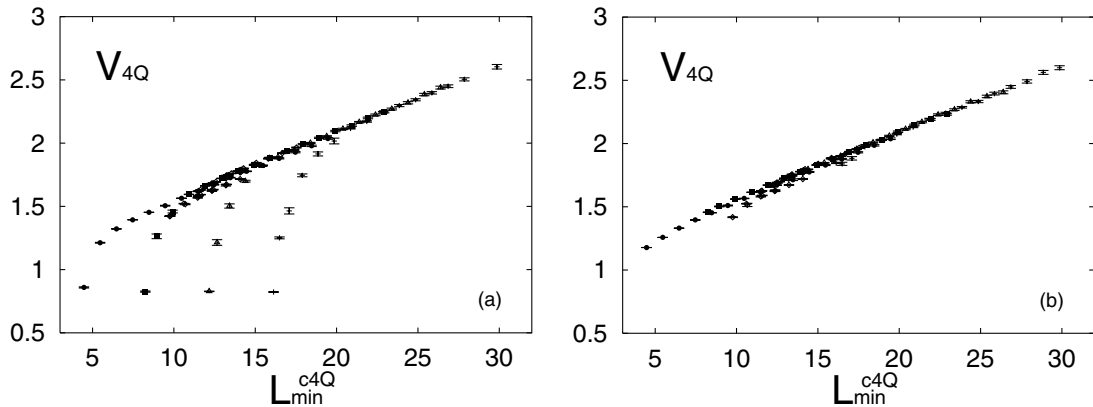

FIG. 11.   The 4Q potential V_{4Q} plotted against $L_{\min}^{c4Q}$ (a) for planar 4Q configurations; (b) for twisted 4Q configurations. $L_{\min}^{c4Q}$ denotes the minimal flux-tube length for the connected 4Q configuration. We plot all the lattice QCD data of V_{4Q} for the symmetric case with $d = 1$ (solid circles), $d = 2$ (solid squares), $d = 3$ (open triangles), and $d = 4$ (crosses) together with the asymmetric case (open diamonds).
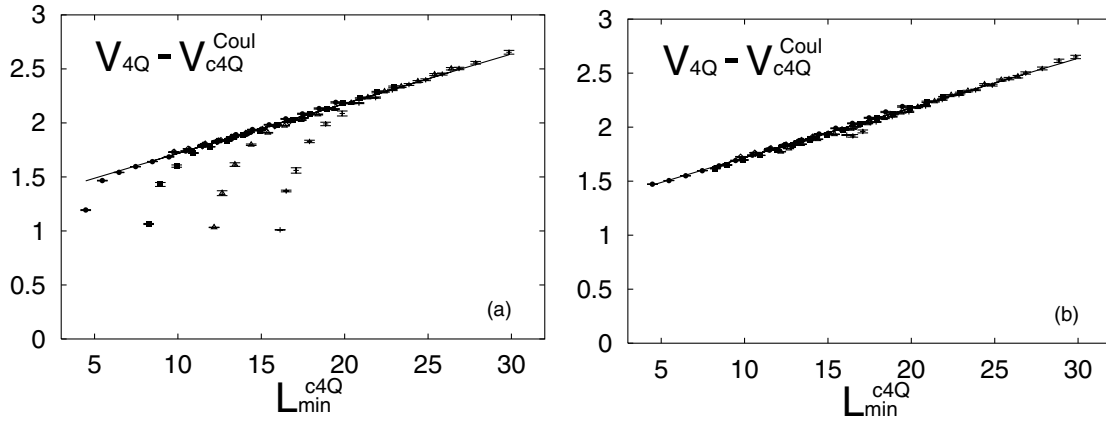
FIG. 12.   The 4Q potential subtracted by the OGE Coulomb part of the connected 4Q system, $V_{4Q} - V_{c4Q}^{Coul}$, plotted against L_{min}^{c4Q} (a) for planar 4Q configurations; (b) for twisted 4Q configurations. We plot all the lattice QCD data including asymmetric cases. The meaning of the symbols is the same as in Fig. 11. The solid line denotes $\sigma_{4Q} L_{min}^{c4Q} + C_{4Q}$.

tube changes its shape so as to have the minimal length, the multi-Y-type flux tube is expected to change into a two-meson state for small h.

This type of flip-flop is physically important for the properties of 4Q states especially for their decay process into two mesons. Note also that, in the flux-tube picture, the meson-meson reaction is described by the flux-tube

recombination between the two mesons, and this process can be realized through the two successive flip-flops between the two-meson state and the connected 4Q state. Therefore, this type of flip-flop is important also for the reaction mechanism between two mesons.

As a clear signal of the flip-flop, we again show the 4Q potential V_{4Q} for the symmetric planar 4Q configuration
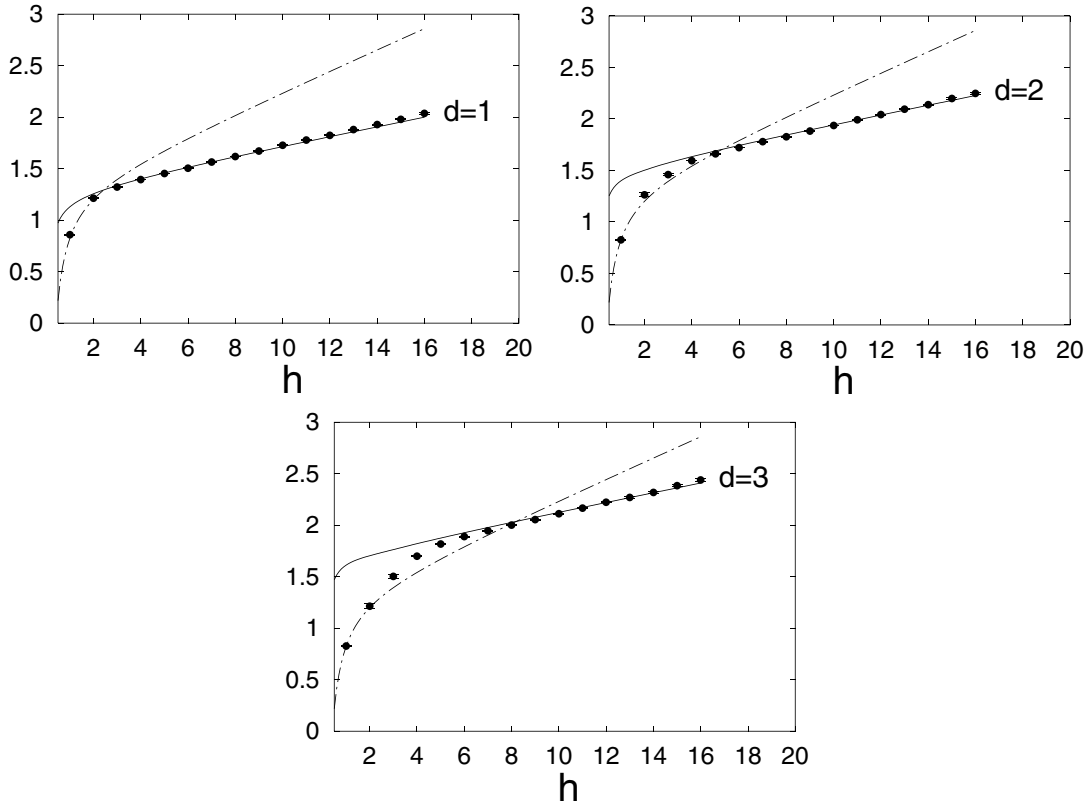

FIG. 13.   The typical lattice QCD results for the flip-flop between the connected 4Q state and the two-meson state for the symmetric planar 4Q configuration with fixed d. The symbols denote lattice QCD results. The curves describe the theoretical form: the solid curves denote the OGE plus multi-Y Ansatz, and the dash-dotted curve the two-meson Ansatz.

with $d = 1, 2, 3$ separately in Fig. 13. The solid curves denote V_{c4Q} for the OGE plus multi-Y Ansatz, and the dash-dotted curves $V_{2Q\bar{Q}} = 2V_{Q\bar{Q}}(h)$ for the two-meson Ansatz. For large h, V_{4Q} coincides with the energy V_{c4Q} of the connected 4Q system. For small h, V_{4Q} coincides with the energy $2V_{Q\bar{Q}}$ of the two-meson system composed of two flux tubes. In the intermediate region of h, one can observe the crossover from one Ansatz to another.

Thus, in these particular cases, we can observe a clear evidence of the flip-flop as

$$V_{4Q}(d, h) \simeq \min(V_{c4Q}(d, h), 2V_{Q\bar{Q}}(h)), \qquad (24)$$

which indicates the transition between the connected 4Q state and the two-meson state around the level-crossing point where these two systems are degenerate as $V_{c4Q}(d, h) = 2V_{Q\bar{Q}}(h)$. This result also supports the flux-tube picture even for the 4Q system.

The present lattice QCD results on the flip-flop lead to infrared screening and disappearance of the long-range color interactions, i.e., the confining force and the OGE Coulomb force, between (anti)quarks belonging to different "mesons." This physically results in the absence of the tree-level color van der Waals force between two mesons [62–64].

VI. SUMMARY AND CONCLUDING REMARKS

We have performed the detailed study of the tetraquark (4Q) potential V_{4Q} for various QQ-$\bar{Q}\bar{Q}$ systems in SU(3) lattice QCD with $\beta = 6.0$ and $16^3 \times 32$ at the quenched level. For about 200 different patterns of 4Q systems, we have extracted V_{4Q} from the 4Q Wilson loop in 300 gauge configurations, with the smearing method to enhance the ground-state component. We have calculated V_{4Q} for planar, twisted, asymmetric, and large-size 4Q configurations, respectively. The calculation for large-size 4Q configurations has been done by identifying $16^2 \times 32$ as the spatial size and 16 as the temporal one, and the long-distance confinement force has been particularly analyzed in terms of the flux-tube picture.

When QQ and $\bar{Q}\bar{Q}$ are well separated, V_{4Q} is found to be expressed as the sum of the one-gluon-exchange Coulomb term and multi-Y-type linear term based on the flux-tube picture. In this case, all four quarks are linked by the connected double-Y-shaped flux tube, where the total flux-tube length is minimized. On the other hand, when the nearest quark and antiquark pair is spatially close, the system is described as a two-meson state rather than the connected 4Q state.

We have observed a flux-tube recombination called a flip-flop between the connected 4Q state and the two-meson state around the level-crossing point. This flip-flop leads to infrared screening of the long-range color interactions between (anti)quarks belonging to different mesons

and results in the absence of the tree-level color van der Waals force between two mesons.

As a next step, it is interesting to investigate the transition in terms of the level crossing between the connected 4Q state and the two-meson state through the diagonalization of the correlation matrix with various 4Q states [34]. Through the investigation of the excited-state levels of the 4Q system, a realistic picture for the reaction mechanism between two mesons may be obtained.

The dynamical quark effect for the flux-tube picture and the flip-flop would be also an interesting subject. In this context, the string-breaking effect may cause a more complicated variation of the transition between the single $Q\bar{Q}$ meson and the multiquark system.

In any case, recent lattice QCD studies begin to shed light on the realistic picture in hadron physics and to reveal even the properties of the multiquark system.

APPENDIX: OGE COULOMB TERMS IN THE 4Q POTENTIAL

In the Appendix, we briefly show the derivation of the OGE Coulomb terms in the 4Q potential in Eq. (5) by calculating $\langle T | T_i^a T_j^a | T \rangle$ for the 4Q state $|T\rangle$.

In the quark picture, the 4Q state $|T\rangle$ corresponding to Fig. 2 is expressed as

$$|T\rangle = |(Q_1 Q_2)_{\bar{3}} (\bar{Q}_3 \bar{Q}_4)_3\rangle_1$$
$$= \frac{1}{2\sqrt{3}} \epsilon^{abc} \epsilon^{ab'c'} |Q_1^b Q_2^c \bar{Q}_3^{b'} \bar{Q}_4^{c'}\rangle, \qquad (A1)$$

where the indices denote the SU(3) color indices of (anti)-quarks. Here, $|T\rangle$ is normalized as

$$\langle T \mid T \rangle = \frac{1}{12} \epsilon^{abc} \epsilon^{ab'c'} \epsilon^{def} \epsilon^{de'f'} = 1. \qquad (A2)$$

The color matrix factor $T_i^a T_j^a$ in the OGE process can be expressed with the Casimir operator $C_2(R)$ as

$$T_i^a T_j^a = \frac{1}{2}\{(T_i^a + T_j^b)^2 - (T_i^a)^2 - (T_j^a)^2\}$$
$$= \frac{1}{2}\{C_2(R_{i+j}) - C_2(R_i) - C_2(R_j)\}$$
$$= \frac{1}{2} C_2(R_{i+j}) - \frac{4}{3}, \qquad (A3)$$

where R_{i+j} denotes the total SU(3) color representation of

the $(i + j)$ system. Here, $C_2(R_i) = C_2(R_j) = \frac{4}{3}$ has been used for each (anti)quark belonging to **3** (**3̄**).

In this 4Q system, the two quarks, Q_1 and Q_2, form the **3̄** representation, i.e., $C_2(R_{1+2}) = C_2(\bar{\mathbf{3}}) = \frac{4}{3}$, and then one gets $\langle T | T_1^a T_2^a | T \rangle = -\frac{2}{3}$. This type of the Coulomb coefficient between two quarks is the same as that in the 3Q system. Similarly, one gets $\langle T | T_3^a T_4^a | T \rangle = -\frac{2}{3}$ for the two antiquarks, $\bar{Q}_3$ and $\bar{Q}_4$.

Next, we consider the Coulomb interaction between the quark and the antiquark. Owing to the symmetry, we only have to investigate the interaction between Q_1 and $\bar{Q}_3$. To this end, we rewrite the 4Q state $|T\rangle$ in terms of the irreducible representation for the $Q_1 + \bar{Q}_3$ system. Since Q_1 and $\bar{Q}_3$ can form the singlet (**1**) or the octet (**8**) representation, the 4Q state $|T\rangle$ can be rewritten as

$$|T\rangle = C_1 |(Q_1\bar{Q}_3)_1 (Q_2\bar{Q}_4)_1\rangle + C_8 |(Q_1\bar{Q}_3)_8 (Q_2\bar{Q}_4)_8\rangle_1 \tag{A4}$$

with appropriate constants C_1 and C_8 satisfying

$$|C_1|^2 + |C_8|^2 = 1. \tag{A5}$$

After some calculation, one finds

$$|\mathbf{11}\rangle \equiv |(Q_1\bar{Q}_3)_1 (Q_2\bar{Q}_4)_1\rangle = \frac{1}{3} |Q_1^a Q_2^b \bar{Q}_3^b \bar{Q}_4^b\rangle, \tag{A6}$$

$$|\mathbf{88}\rangle \equiv |(Q_1\bar{Q}_3)_8 (Q_2\bar{Q}_4)_8\rangle_1$$
$$= \frac{1}{2\sqrt{2}} \left\{ |Q_1^a Q_2^b \bar{Q}_3^b \bar{Q}_4^a\rangle - \frac{1}{3} |Q_1^a Q_2^b \bar{Q}_3^a \bar{Q}_4^b\rangle \right\}, \tag{A7}$$

which satisfy the orthonormal condition,

$$\langle \mathbf{11} | \mathbf{11} \rangle = \langle \mathbf{88} | \mathbf{88} \rangle = 1, \qquad \langle \mathbf{11} | \mathbf{88} \rangle = 0. \tag{A8}$$

Using Eqs. (A1), (A6), and (A7), C_1 and C_8 can be obtained as

$$C_1 = \langle \mathbf{11} | T \rangle$$
$$= \frac{1}{6\sqrt{3}} \epsilon^{abc} \epsilon^{ab'c'} \langle Q_1^d Q_2^e \bar{Q}_3^d \bar{Q}_4^e | Q_1^b Q_2^c \bar{Q}_3^{b'} \bar{Q}_4^{c'} \rangle$$
$$= \frac{1}{6\sqrt{3}} \epsilon^{abc} \epsilon^{abc} = \frac{1}{\sqrt{3}}, \tag{A9}$$

$$C_8 = \langle \mathbf{88} | T \rangle$$
$$= \frac{1}{4\sqrt{6}} \epsilon^{abc} \epsilon^{ab'c'} \langle Q_1^d Q_2^e \bar{Q}_3^e \bar{Q}_4^d | Q_1^b Q_2^c \bar{Q}_3^{b'} \bar{Q}_4^{c'} \rangle$$
$$\quad - \frac{1}{12\sqrt{6}} \epsilon^{abc} \epsilon^{ab'c'} \langle Q_1^d Q_2^e \bar{Q}_3^d \bar{Q}_4^e | Q_1^b Q_2^c \bar{Q}_3^{b'} \bar{Q}_4^{c'} \rangle$$
$$= \frac{1}{4\sqrt{6}} \epsilon^{abc} \epsilon^{acb} - \frac{1}{12\sqrt{6}} \epsilon^{abc} \epsilon^{abc} = -\sqrt{\frac{2}{3}}. \tag{A10}$$

Then, using Eq. (A1), $C_2(\mathbf{1}) = 0$ and $C_2(\mathbf{8}) = 3$, we get

$$\langle T | T_1^a T_3^a | T \rangle = |C_1|^2 \langle \mathbf{11} | T_1^a T_3^a | \mathbf{11} \rangle + |C_8|^2 \langle \mathbf{88} | T_1^a T_3^a | \mathbf{88} \rangle$$
$$= |C_1|^2 \left\{ \frac{1}{2} C_2(\mathbf{1}) - \frac{4}{3} \right\} + |C_8|^2 \left\{ \frac{1}{2} C_2(\mathbf{8}) - \frac{4}{3} \right\}$$
$$= -\frac{1}{3}. \tag{A11}$$

In this way, for the Coulomb interaction in the 4Q system as shown in Fig. 3, we obtain

$$\langle T | T_1^a T_2^a | T \rangle = \langle T | T_3^a T_4^a | T \rangle = -\frac{2}{3}, \tag{A12}$$

$$\langle T | T_1^a T_3^a | T \rangle = \langle T | T_1^a T_4^a | T \rangle = \langle T | T_2^a T_3^a | T \rangle$$
$$= \langle T | T_2^a T_4^a | T \rangle = -\frac{1}{3}, \tag{A13}$$

and derive the Coulomb terms in Eq. (5).

[1] M. Creutz, Phys. Rev. Lett. **43**, 553 (1979); **43**, 890(E) (1979); Phys. Rev. D **21**, 2308 (1980).
[2] For instance, H. J. Rothe, *Lattice Gauge Theories* (World Scientific, Singapore, 1997), 2nd ed., and references therein.
[3] M. Albanese *et al.* (APE Collaboration), Phys. Lett. B **192**, 163 (1987).
[4] G. S. Bali and K. Schilling, Phys. Rev. D **47**, 661 (1993).
[5] T. T. Takahashi, H. Matsufuru, Y. Nemoto, and H. Suganuma, Phys. Rev. Lett. **86**, 18 (2001).
[6] T. T. Takahashi, H. Suganuma, Y. Nemoto, and H. Matsufuru, Phys. Rev. D **65**, 114509 (2002).
[7] T. T. Takahashi and H. Suganuma, Phys. Rev. Lett. **90**, 182001 (2003); Phys. Rev. D **70**, 074506 (2004).
[8] H. Suganuma, H. Ichie, and T. T. Takahashi, in *Proceedings of the International Conference on Color Confinement and Hadrons in Quantum Chromodynamics, RIKEN, Japan, 2003*, edited by H. Suganuma *et al.* (World Scientific, World Scientific, 2004), pp. 249–261.
[9] T. Nakano *et al.* (LEPS Collaboration), Phys. Rev. Lett. **91**, 012002 (2003).
[10] V. V. Narmin *et al.* (DIANA Collaboration), Phys. At. Nucl. **66**, 1715 (2003).
[11] S. Stephanian *et al.* (CLAS Collaboration), Phys. Rev. Lett. **91**, 252001 (2003).
[12] J. Barth *et al.* (SAPHIR Collaboration), Phys. Lett. B **572**, 127 (2003).
[13] A. Aktas *et al.* (H1 Collaboration), Phys. Lett. B **588**, 17 (2004).

[14] C. Alt *et al.* (NA49 Collaboration), Phys. Rev. Lett. **92**, 042003 (2004).

[15] D. Diakonov, V. Petrov, and M. Polyakov, Z. Phys. A **359**, 305 (1997).

[16] For a recent review, S. L. Zhu, Int. J. Mod. Phys. A **19**, 3439 (2004), and references therein.

[17] J. Z. Bai *et al.* (BES Collaboration), Phys. Rev. D **70**, 012004 (2004); I. Abt *et al.* (HERA-B Collaboration), Phys. Rev. Lett. **93**, 212003 (2004); Yu. M. Antipov *et al.* (SPHINX Collaboration), Eur. Phys. J. A **21**, 455 (2004); M. J. Longo *et al.* (HyperCP Collaboration), Phys. Rev. D **70**, 111101 (2004).

[18] S. K. Choi *et al.* (Belle Collaboration), Phys. Rev. Lett. **91**, 262001 (2003).

[19] D. Acosta *et al.* (CDF II Collaboration), Phys. Rev. Lett. **93**, 072001 (2004).

[20] V. M. Abazov *et al.* (D0 Collaboration), Phys. Rev. Lett. **93**, 162002 (2004).

[21] B. Aubert *et al.* (*BABAR* Collaboration), Phys. Rev. Lett. **93**, 041801 (2004).

[22] B. Aubert *et al.* (*BABAR* Collaboration), Phys. Rev. Lett. **90**, 242001 (2003).

[23] P. Krokovny *et al.* (Belle Collaboration), Phys. Rev. Lett. **91**, 262002 (2003).

[24] F. E. Close and S. Godfrey, Phys. Lett. B **574**, 210 (2003).

[25] F. E. Close and P. R. Page, Phys. Lett. B **578**, 119 (2004).

[26] N. A. Tornqvist, hep-ph/0308277.

[27] S. Pakvasa and M. Suzuki, Phys. Lett. B **579**, 67 (2004).

[28] C. Y. Wong, Phys. Rev. C **69**, 055202 (2004).

[29] E. Braaten and M. Kusunoki, Phys. Rev. D **69**, 074005 (2004).

[30] T. Barnes and S. Godfrey, Phys. Rev. D **69**, 054008 (2004).

[31] E. J. Eichten, K. Lane, and C. Quigg, Phys. Rev. D **69**, 094019 (2004).

[32] E. S. Swanson, Phys. Lett. B **588**, 189 (2004); **598**, 197 (2004).

[33] R. L. Jaffe and F. Wilczek, Phys. Rev. Lett. **91**, 232003 (2003).

[34] A. M. Green, J. Lukkarinen, P. Pennanen, and C. Michael, Phys. Rev. D **53**, 261 (1996).

[35] P. Pennanen, A. M. Green, and C. Michael, Phys. Rev. D **59**, 014504 (1999).

[36] F. Okiharu, H. Suganuma, and T. T. Takahashi, Phys. Rev. Lett. **94**, 192001 (2005).

[37] H. Suganuma, T. T. Takahashi, F. Okiharu, and H. Ichie, Nucl. Phys. B Proc. Suppl. **141**, 92 (2005).

[38] H. Suganuma, T. T. Takahashi, F. Okiharu, and H. Ichie, in *Quark Confinement and Hadron Spectrum VI, 2004, Italy*, edited by N. Brambilla *et al.*, AIP Conf. Proc. No. 756 (AIP, New York, 2005), p. 123.

[39] H. Suganuma, F. Okiharu, T. T. Takahashi, and H. Ichie, Nucl. Phys. **A755**, 399 (2005).

[40] H. Suganuma, H. Ichie, F. Okiharu, and T. T. Takahashi, in *Proceedings of the International Workshop on "Pentaquark04," SPring-8, Japan, 2004* (World Scientific, Singapore, 2005), p. 414.

[41] F. Okiharu, H. Suganuma, and T. T. Takahashi, in *Proceedings of the International Workshop on "Pentaquark04," SPring-8, Japan, 2004* (Ref. [40]), p. 339.

[42] C. Alexandrou and G. Koutsou, Phys. Rev. D **71**, 014504 (2005).

[43] J. Weinstein and N. Isgur, Phys. Rev. Lett. **48**, 659 (1982).

[44] Fl. Stancu and D. O. Riska, Phys. Lett. B **575**, 242 (2003).

[45] Y. Kanada-Enyo, O. Morimatsu, and T. Nishikawa, Phys. Rev. C **71**, 045202 (2005); in *Proceedings of the International Workshop on "Pentaquark04," SPring-8, Japan, 2004* (Ref. [40]), p. 239.

[46] R. L. Jaffe, Phys. Rev. D **15**, 267 (1977).

[47] D. Black, A. H. Fariborz, F. Sannino, and J. Schechter, Phys. Rev. D **59**, 074026 (1999).

[48] M. Alford and R. L. Jaffe, Nucl. Phys. **B578**, 367 (2000).

[49] Y. Nambu, Phys. Rev. D **10**, 4262 (1974).

[50] J. Kogut and L. Susskind, Phys. Rev. D **11**, 395 (1975).

[51] J. Carlson, J. Kogut, and V. Pandharipande, Phys. Rev. D **27**, 233 (1983); **28**, 2807 (1983).

[52] A. Casher, H. Neuberger, and S. Nussinov, Phys. Rev. D **20**, 179 (1979).

[53] N. Isgur and J. Paton, Phys. Lett. **124B**, 247 (1983); Phys. Rev. D **31**, 2910 (1985).

[54] A. Patel, Nucl. Phys. **B243**, 411 (1984); Phys. Lett. **139B**, 394 (1984).

[55] M. Oka, Phys. Rev. D **31**, 2274 (1985); M. Oka and C. J. Horowitz, Phys. Rev. D **31**, 2773 (1985).

[56] F. Lenz, J. T. Londergan, E. J. Moniz, R. Rosenfelder, M. Stingl, and K. Yazaki, Ann. Phys. (N.Y.) **170**, 65 (1986).

[57] H. Ichie, V. Bornyakov, T. Streuer, and G. Schierholz, Nucl. Phys. **A721**, C899 (2003); Nucl. Phys. B Proc. Suppl. **119**, 751 (2003).

[58] V. G. Bornyakov, H. Ichie, Y. Mori, D. Pleiter, M. I. Polikarpov, G. Schierholz, T. Streuer, H. Stüben, and T. Suzuki, Phys. Rev. D **70**, 054506 (2004).

[59] P. O. Bowman and A. P. Szczepaniak, Phys. Rev. D **70**, 016002 (2004).

[60] D. S. Kuzmenko and Yu. A. Simonov, Phys. At. Nucl. **66**, 950 (2003).

[61] J. M. Cornwall, Phys. Rev. D **69**, 065013 (2004).

[62] T. Appelquist and W. Fischler, Phys. Lett. **77B**, 405 (1978).

[63] M. B. Gavela, A. Le Yaouanc, L. Oliver, O. Pene, J. C. Raynal, and S. Sood, Phys. Lett. **82B**, 431 (1979).

[64] G. Feinberg and J. Sucher, Phys. Rev. D **20**, 1717 (1979).